Int. J. Electrochem. Sci., 12 **(2017)** 3614 – 3634, doi: 10.20964/2017.05.24

International Journal of
ELECTROCHEMICAL
SCIENCE
www.electrochemsci.org

Correlation between Anti-Corrosion Performance and Optical Reflectance of Nano Fluoride Film on Biodegradable Mg-Zn-Zr Alloy: a Non-Destructive Evaluation Approach

Da-Jun Lin[1], *Fei-Yi Hung*[1,*], *Ming-Long Yeh*[2], *Hung-Pang Lee*[2], *Truan-Sheng Lui*[1]

[1] Department of Materials Science and Engineering, National Cheng Kung University, Tainan 701, TAIWAN.
[2] Department of Biomedical Engineering, National Cheng Kung University, Tainan 701, TAIWAN.
[*]E-mail: fyhung@mail.ncku.edu.tw

Received: 11 February 2017 / *Accepted:* 5 March 2017 / *Published:* 12 April 2017

Magnesium alloy is promising new biomaterial due to its satisfactory mechanical performance, biocompatibility and degradation of non-toxic substances. However, the dual problems of corrosion and hydrogen evolution require overcoming in order to reach a practical application level. For anti-corrosion modification, fluoride conversion treatment was chosen to provide varied MgF_2 coatings on the microstructure-modified Mg-Zn-Zr alloy The aim of the present study was to investigate the influence of coating structures and their corresponding corrosion resistance. The fluoride coatings were constructed with nano-crystalline composites, which demonstrated that Mg-Zn precipitates participate in the coating-growth mechanism. In addition, the improved corrosion resistance was also systematically investigated. Compared with the pristine substrate, the F24h and F48h specimens significantly improved the anti-corrosion performance. Moreover, this report is the first report to propose a non-destructive evaluation method through simultaneous evaluation of the corrosion behavior and the establishment of a correspondence surface reflectance for fluoride conversion coatings on Mg-Zn-Zr alloy.

Keywords: Magnesium alloy, fluoride conversion coating, anti-corrosion, optical reflectance

1. INTRODUCTION

Magnesium is a widely acknowledged essential mineral nutrient needed for maintenance of metabolism and physiological functions [1, 2]. Nowadays, magnesium and its alloys, such as the Mg-Zn series and Mg-Ca series, are being developed as a potential candidate for a new generation of biodegradable implant materials [3-6], especially for use in the orthopedic and cardiovascular fields. However, the major obstacle of magnesium alloys for biomedical applications is the rapid corrosion

reaction in physiological electrolytic environments [7]. If severe corrosion occurs on the magnesium surface, it could possibly lead to significant oxidation reaction and hydrogen gas evolution [8], which would cause adverse effects on adjacent cells and/or tissues. Moreover, in an ideal situation, the degradation rate of a magnesium implant must be synchronized to that of the tissue healing rate to ensure that functionality is maintained during the implantation period [9]. Currently, modification of the anti-corrosion performance for bio-magnesium alloys is the most important issue.

To address the aforementioned concerns, an increasing number of reports have developed toxicity-free alloy compositions, microstructure-modified matrices and surface modification methods using various engineering techniques [10-12]. Ceramic conversion coating treatments are commonly applied to the magnesium surface, such as chromate conversion [13], fluoride conversion [14, 15], phosphate conversion, and others [16-20]. Among these treatments, fluoride conversion has great potential. Chiu et al. reported that a uniform protective coating of about 1.5 μm thick was formed on pure magnesium by immersion in 48 wt.% HF for 24h [21]. Moreover, Farley et al. reported that treatment with fluoride increased the proliferation and alkaline phosphatase activity of bone cells in vitro; in addition, such treatment also increased bone formation in embryonic calvarias at concentrations that stimulate bone formation in vivo [22]. That is to say, the fluoride-coated magnesium surface not only possessed good anti-corrosion ability but also provided a suitable environment for bone-related cells. Until now, fluoride coating related studies have only focused on pure Mg, Mg-Al [14], Mg-Ca [23] and Mg-Li series alloys [24].

Mg-Zn series alloys are mainly composed of non-toxic Mg and Zn elements, and it has been reported that Mg-Zn alloys exhibit acceptable biocompatibility [4]. In this study, we used a microstructure-modified Mg-Zn-Zr alloy that combines the advantages of toxicity-free composition and optimized microstructure [10]. In spite of its improved degradation behavior and excellent cytocompatibility, the problem of hydrogen gas remained. Therefore, a fluoride conversion coating was employed to modify the surface properties of the microstructure-modified magnesium alloy. The coating formation behaviors, material properties and electrochemical corrosion mechanism of the fluoride conversion film were investigated in detail. In addition, the optical properties of the fluoride films on the microstructure-modified Mg-Zn-Zr alloy were also established and compared with the corresponding electrochemical results to construct an anti-corrosion performance index for non-destructive analysis.

2. MATERIALS AND METHODS

2.1 Materials and surface treatment

Circular samples (with a diameter of 12 mm) were cut from extruded Mg-Zn-Zr (ZK60) alloy. All specimens were vacuum heat treated at 400^{o}C with a previously reported process, and then polished successively with 200 to 8000 grit using SiC sandpaper. The polished specimens were rinsed in acetone and ethanol, and subsequently dried in a stream of air (named as ZK60H). For the fluoride conversion treatment, the ZK60H samples were soaked in 42wt.% HF and placed in an orbital shaker at 90 rpm for various time periods (1h, 6h, 24h and 48 h). After the specimens were removed from the HF bath, they were rinsed two times with 95% ethanol and dried. Names of the surface-treated samples

were assigned according to treatment period, hereafter referred to as F1h, F6h, F24h and F48h, respectively.

2.2 Material characterization

The surface characteristics and cross-section profile of the fluoride coating were examined using ultra high resolution scanning electron microscopy (UHR-SEM, Auriga, Carl Zeiss). To better reveal the coating formation, the F/Mg ratio of the samples was determined using an energy dispersive spectrometer (EDS, Oxford). To characterize the phase structure of the fluorinated ZK60H, a grazing incidence X-ray diffractometer (GI-XRD, D8 discover, Bruker) with CuKα radiation (λ=0.154 nm) was utilized in this study. The diffraction patterns were acquired between the 2θ values of 20~80° with a scanning speed of 4° min^{-1}. The freshly prepared F24h specimen was chosen for crystalline and coating structure analysis, using DB-FIB(Dual-beam Focus Ion Beam, FEI Nova 200) to produce a 10 μm × 5 μm × 40 nm TEM sample. The microstructure image and elemental distribution of F24h were acquired through a field-emission transmission electron microscope (FE-TEM, FEI Tecnai G2). The optical characteristics (reflectance spectra) of the fluoride films were measured in the 200~800nm region using a spectrophotometer (U3010, Hitachi) equipped with a halogen light source.

2.3 Electrochemical corrosion test

The electrochemical corrosion mechanism and coating performance of the fluoride conversion coating were investigated using an electrochemical station (PARSTAT 2273, Princeton Applied Research). Polarization curves and electrochemical impedance spectra (EIS) were measured using a classic three-electrode cell. A saturated calomel electrode (SCE, +0.242 V vs. SHE) was used as the reference electrode with a Pt-coated Ti mesh as the counter-electrode. The area of the working electrode exposed to the electrolyte was controlled to within 1 cm^2 by a Teflon holder. The electrolyte used was revised simulated body fluid (r-SBF) solution (per liter, included 5.403 g of NaCl, 0.736 g of $NaHCO_3$, 2.036 g of Na_2CO_3, 0.225 g of KCl, 0.182 g of K_2HPO_4, 0.310 g of $MgCl_2 \cdot 6H_2O$, 11.928 g of 4-(2-hydroxyethyl)-1-piperazineethanesulfonic acid (HEPES), 0.293 g of $CaCl_2$, 0.072 g of Na_2SO_4 dissolved in deionized (DI) water.) buffered at pH=7.4 using HEPES and NaOH, the environmental temperature of which was controlled at 37°C. Prior to conducting the experiment, nitrogen gas was bubbled through the r-SBF to remove dissolved oxygen. The polarization curve was acquired with a scanning rate of 1 mV s^{-1} from −1.8 V to −0.8 V, while the electrochemical impedance spectra (EIS) were obtained at the corrosion potential in the frequency range between 10 kHz to 10 mHz, with a signal amplitude of 10 mV.

2.4 Immersion and hydrogen evolution test

The immersion tests were employed to understand the corrosion results and tendencies in r-SBF by following the principle of ASTM G31-72. The r-SBF volume to surface area ratio was fixed at

20 mL/cm^2. All experimental samples were removed after 1 week of immersion, after which the corroded surfaces were examined by SEM. For the hydrogen evolution test, the previously reported equipment was used to evaluate the hydrogen evolution volume. The experimental environment and solution volume-to-surface-area ratio were fixed at 37 ^{o}C in a water bath and 100 mL/cm^2, respectively.

3. RESULTS AND DISCUSSION

3.1. Coating characteristics

It is well established that MgF_2 coatings deposited from 42 wt.% HF solution have a dark appearance (Fig. 1a).

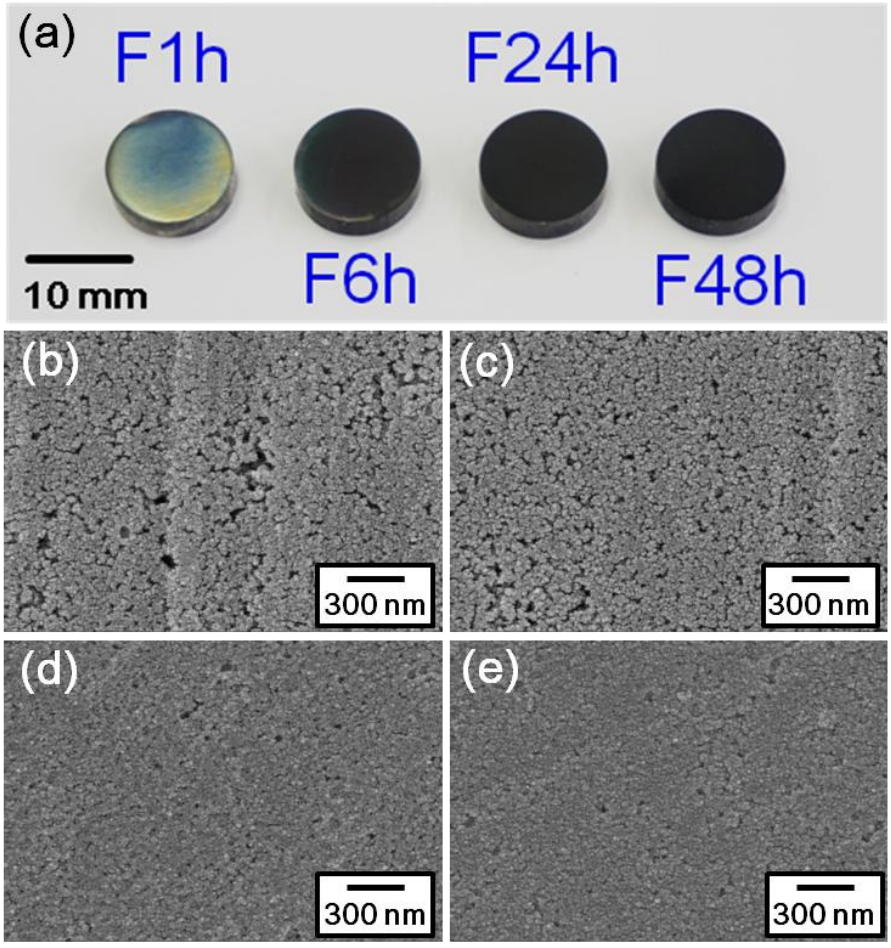

Figure 1. Surface macrograph and micrographs of the samples fluorinated for different conversion times: (a): appearance of each specimen, (b) F1h specimen, (c) F6h specimen, (d) F24h specimen, and, (e) F48h specimen.

The images suggest that the surface color evolved to deep black when the coating period exceeded 6h. The surface morphology reveals that the MgF_2 coatings were formed by nanoparticle

deposition (Fig. 1b~1e), the average nanoparticle diameter of which was around 30nm. At the beginning of the conversion process (F1h and F6h), the MgF_2 nanoparticles were unevenly distributed on the surface, leading to a pore-rich microstructure. By prolonging the reaction time (F24h and F48h), the surface defects and pores reduced significantly, suggesting that the surface pores would be gradually sealed by further MgF_2 nanoparticle coverage.

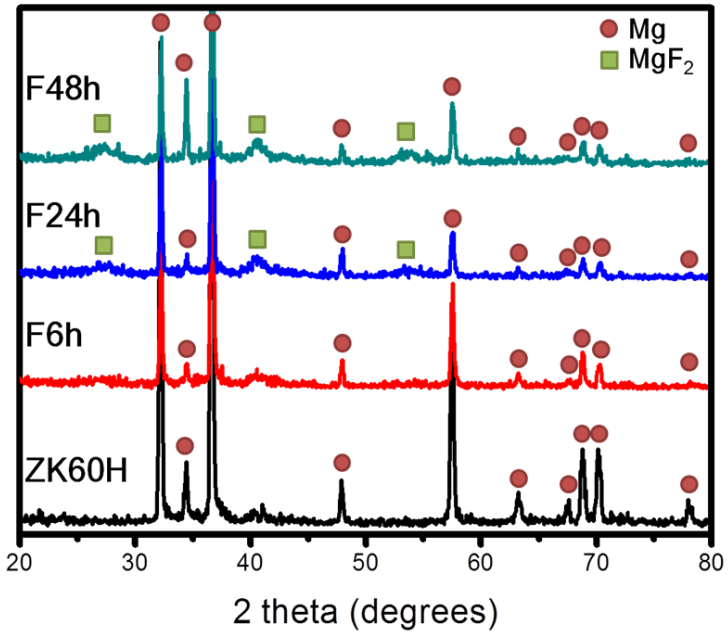

Figure 2. XRD patterns of fluorinated surfaces for different conversion times.

To better understand the coating characteristics, XRD and EDS were utilized to analyze the crystal structure and F/Mg coating ratios with different conversion times. As seen in Fig. 2, the diffraction peaks at 2θ = 27.5°, 40.4° and 53.5° were sharper as the conversion time increased, which indicated that the thickness and crytallinity of MgF_2 coating were enhanced. In addition, the TF-XRD results implied that the MgF_2 coating gradually became more complete and thicker after long immersion periods. Furthermore, it can be seen that the F/Mg ratio gradually increased as the conversion time was prolonged, with saturation occurring after 24h, reaching the stoichiometric ratio (Fig. 3). The growth reactions of the fluoride conversion coating on the magnesium surface are described in the following:

1. $Mg \rightarrow Mg^{2+} + 2e^-$ Eq.1
2. $2H_2O+2e^- \rightarrow H_2+2OH^-$ Eq.2
3. $Mg^{2+} + 2F^- \rightarrow MgF_2\downarrow$, ΔG= -58.65kJ Eq.3
4. $Mg^{2+} + 2OH^- \rightarrow Mg(OH)_2\downarrow$, ΔG= -64.51kJ Eq.4
5. $Mg(OH)_2 + 2HF \rightarrow 2H_2O + MgF_2\downarrow$, ΔG= -232.14kJ Eq.5

When magnesium is immersed in hydrofluoric acid solution, the major oxidation reaction is the dissolution of the α-Mg matrix. The corresponding cathodic reaction occurs during the cathodic phase, which produces hydrogen gas and hydroxyl ions as the main products; further, magnesium hydroxide

will be precipitated through the following reactions and deposited on the surface during the initial stage of coating formation. Despite Eq. 3 also being a spontaneous reaction, the Gibbs-free energy shows a lower possibility of occurring (compared with Eqs. 4 and 5). The spontaneous reaction will decompose magnesium hydroxide and then produce magnesium fluoride compounds when the magnesium hydroxide contacts hydrofluorine molecules.

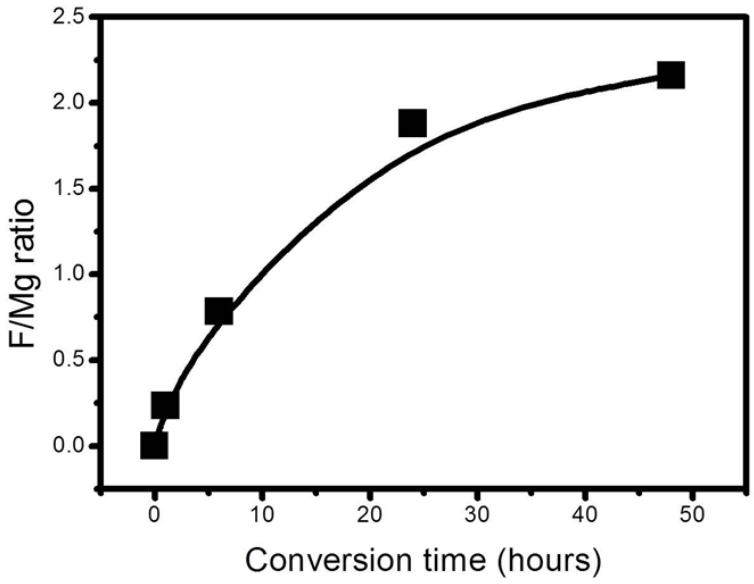

Figure 3. F/Mg ratio obtained by EDS.

Fig. 4a demonstrates the quantitative results for the coating thickness as a function of conversion time, derived from Figs. 3b~d. The initial high reactivity of the bare ZK60H surface showed a quick growth rate in coating thickness. Notably, there was no crack formation or coating delamination on the surface or in the cross-sections of all experimental specimens. Moreover, the thickened MgF_2 layer slowed the MgF_2 deposition process, resulting in sluggish growth in terms of thickness after 24h conversion. Regarding the deposition process of MgF_2 after 24h immersion, the decrease of the surface porosity was associated with a sealing effect. The similar outcomes of pore forming and sealing behavior were also discovered in AZ31B and Mg-Ca alloy in other reports [25, 26]. These surface micro-pores probably acted as a kind of diffusion path for divalent Mg ions to diffuse from substrate to the surface and/or the sub-surface, which played a key role in conversion kinetic process for sealed coating. The presence of the sealing phenomenon can be explained in that the matrix delivered Mg ions through micro-pores to form new MgF_2 nano-particles at the location of the micro-pores during the later deposition period. Notably, the condition of alloy substrate (eg. as-casted or homogenized) is also a important factor which can probably affect the film structuring behaviors and final performance [27, 28]. The previously mentioned reports of this field were only focused in the functional performance and partial surface characteristics without considering the substrate condition. In this research, the ZK60H was modified by homogenization heat treatment. The Mg matrix absorbed massive alloying element and further formed strengthening precipitates [3, 29, 30].

Therefore, the microstructure of fluoride coating should be investigated for realizing the effect of substrate microstructure on coating mechanisms.

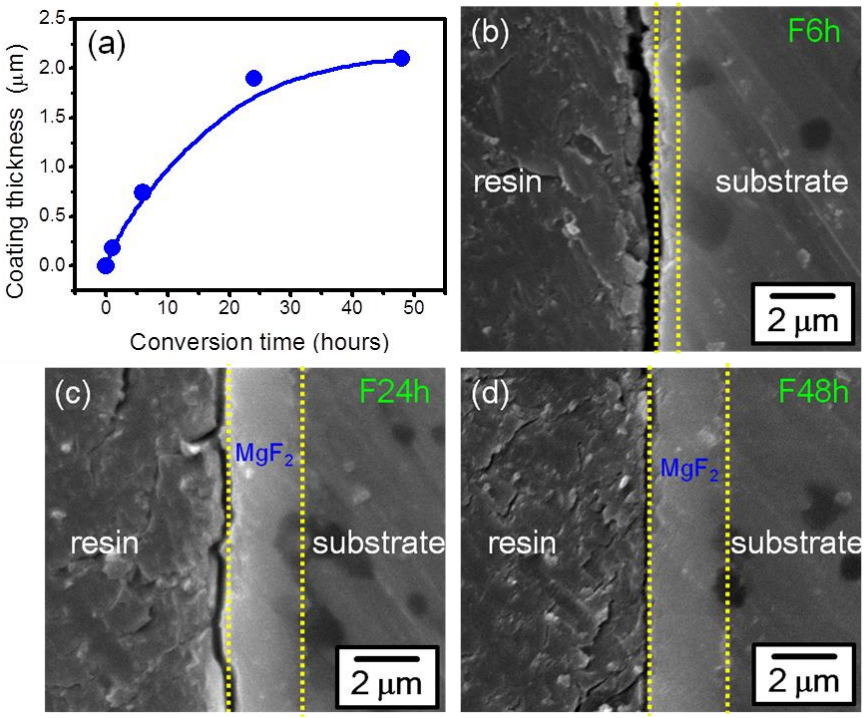

Figure 4. Cross-section profiles of the fluorinated surfaces.

The TEM micrograph and selected area electron diffraction (SAED) patterns for structural and crystallinity observation of the F24h are shown in Fig. 5. The structure of the F24h specimen can be clearly divided into an MgF_2 layer and ZK60H substrate. It can be seen that the few $MgZn_2$ phases distribute randomly on the grain boundaries, and that numerous nanometer-sized $MgZn_2$ precipitates are present in the α-Mg matrix. $MgZn_2$ precipitates can also be preserved in the MgF_2 layer, which indicates that the HF acid conversion of the Mg-Zn alloys is selective, possibly because of the relatively lower chemical activity of $MgZn_2$ than α-Mg. According to a previous study, the micro-galvanic effect between the α-Mg matrix and the cathodic phase dominates in the oxidation process [31], wherein the observed $MgZn_2$ precipitates and surrounding Mg matrix serve as a cathode and anode, respectively. In view of previous discussion, the oxidation of surrounding Mg matrix is firstly occurred in conversion process ($Mg^{2+} + 2OH^- \rightarrow Mg(OH)_2\downarrow$). The reduction reaction simultaneously takes place in the $MgZn_2$ phase, during which gaseous hydrogen appeared to be generated and preferentially distributed in the normal direction. To further stabilize surface and decrease the Gibbs free energy, the fluorine ions and $Mg(OH)_2$ converted to form protective MgF_2 nano-crystallite. Moreover, some partly fluorinated Mg granules (marked by green dash line) were clearly observed, existing near the interface. To investigate further, the zinc constituent in the MgF_2 layer was analyzed by EDS, as shown in Fig.5b. Evidently, the zinc participates in the coating-structure characteristics, for which the zinc elements are gradually distributed in the MgF_2 layer in a progressive gradient.

Moreover, the SAED analysis of the coating indicates that the MgF_2 layer was composed by the polycrystalline tetragonal MgF_2 and hexagonal $MgZn_2$ phases (Fig. 5c). The polycrystalline rings in the SAED pattern correspond to the (301), (220), (211), (201), (110), (103), (202), (206), and (224) lattice planes, respectively, which is in agreement with the coexisting crystalline structures of MgF_2 and $MgZn_2$ (JCPD card no. 00-041-1443 and 71-1177). This report firstly discovered that the MgZn alloying precipitates participated in fluoride coating formation and formed a nano composite film.

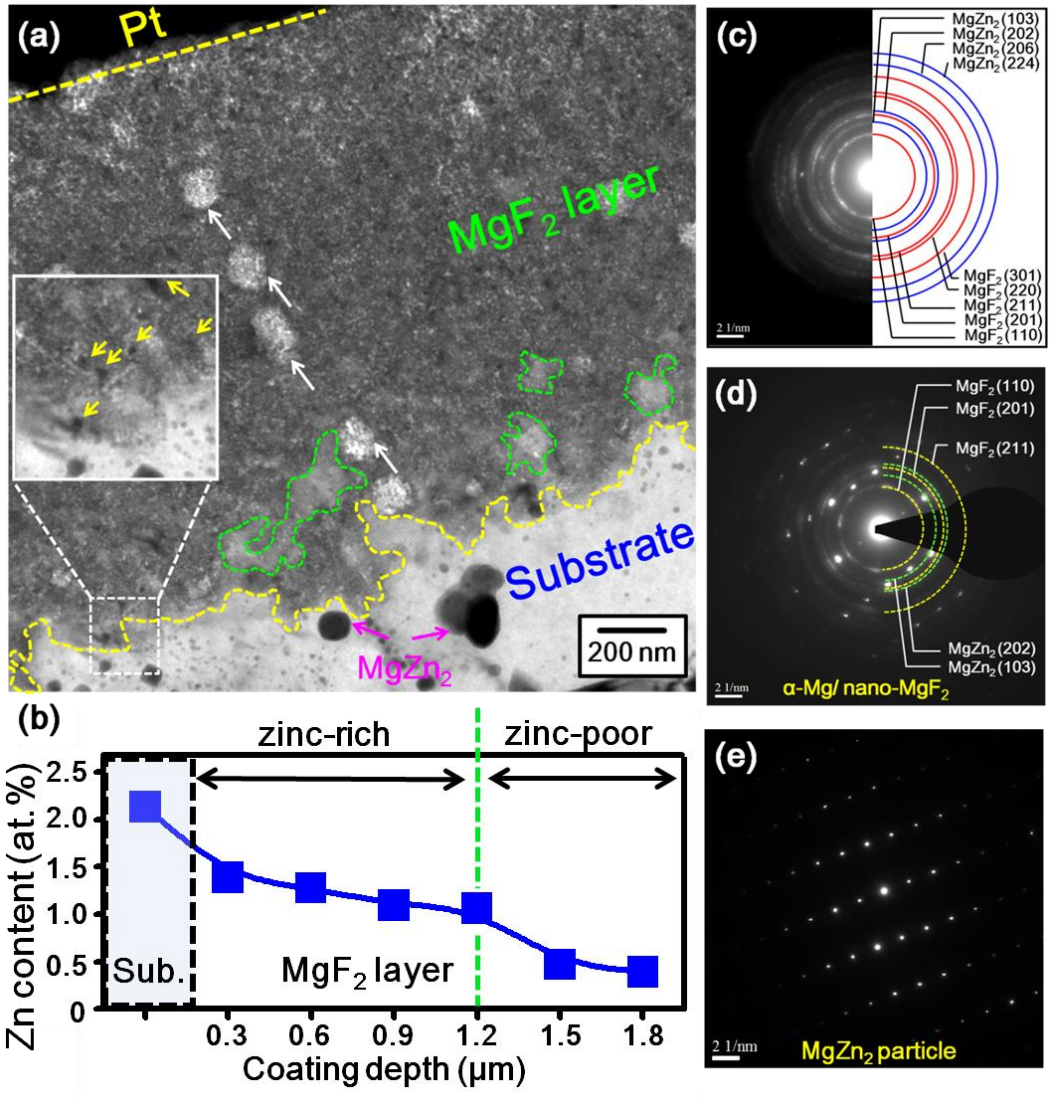

Figure 5. TEM analysis of the F24h specimen (a) cross-section image, and, (b) zinc element distribution profile. SAED patterns of (c) MgF_2 layer, (d) partly fluorinated granule (marked by green dashed line), and (e) $MgZn_2$ particle (marked by pink arrow).

3.2 Corrosion behaviour

In-vitro electrochemical corrosion tests are commonly used to estimate the anti-corrosion performance of biodegradable magnesium alloys [32]. In general, the cathodic reaction mentioned

above is the main water-reduction reaction, which is related to the driving force of hydrogen evolution [33]. The anodic reaction represents the dissolution and oxidation of the α-Mg matrix.

Fig.6 shows the typical polarization curves of each specimen in the r-SBF solution at 37°C. As indicated, both the cathodic and anodic current densities were reduced in the presence of the MgF_2 coating, indicating that such coatings improved the anti-corrosion ability of ZK60H. The corrosion potential and corrosion current density are often applied to evaluate the corrosion resistance, and can be derived via the extrapolation method from the Tafel region. The polarization resistance (R_p) can be calculated using the Stern–Geary equation [34] and the percentage protection efficiency (PE%) [35] from the following equation, which are also listed in table.1

$$R_p = \frac{\beta_a \beta_c}{2.303(\beta_a + \beta_c) I_{corr}}$$

$$PE\ (\%) = \frac{I_{corr,ZK60H} - I_{corr,\ MgF_2}}{I_{corr,ZK60H}} \times 100\%$$

where I_{corr} is the corrosion current density, while β_a and β_c are the anodic and cathodic slopes, respectively, as obtained from the Tafel region.

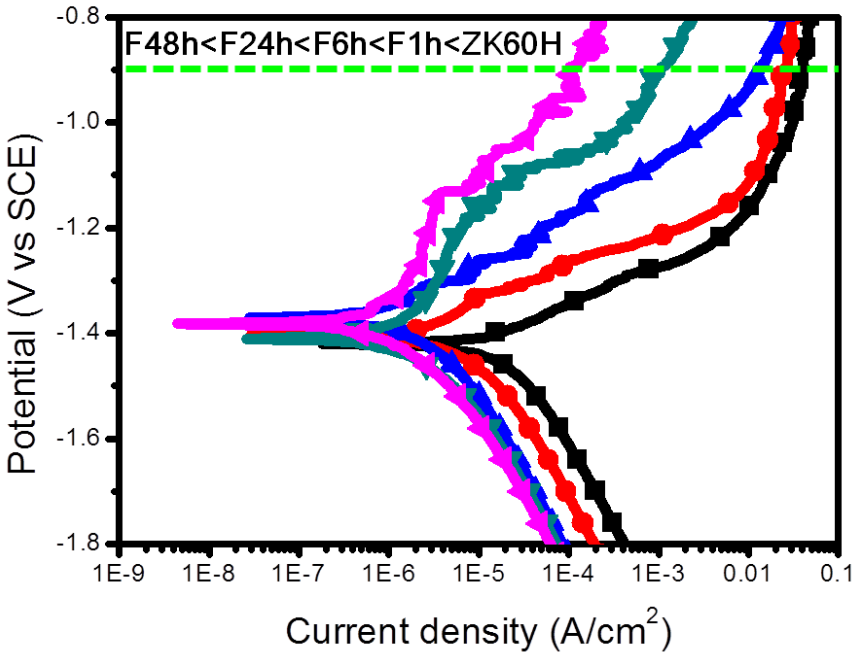

Figure 6. Electrochemical polarization curves obtained in r-SBF solution at 37°C.

According to the above equation, both R_p and PE are inversely proportional to I_{corr}; and, the corrosion current density of all experimental groups constituted the following order: ZK60H **>** F1h **>** F6h **>** F24h ≧ F48h. As expected, because the surface is coated with low conductivity materials, the corrosion current density is related to the coverage status of MgF_2, which can hinder electron exchanges with the environment and reduce micro-galvanic couples [36].

Table 1. The resultant electrochemical polarization parameters.

	E_{corr} (V)	I_{corr} (A/cm^2)	$\beta_{cathodic}$ (V/dec)	β_{anodic} (V/dec)	Rp (Ω-cm^2)	PE%	Porosity%
ZK60H	-1.43	3.7×10^{-5}	0.30	0.13	1123	---	---
F1h	-1.41	1.2×10^{-5}	0.32	0.48	7150	68.6%	13.3%
F6h	-1.38	8.4×10^{-6}	0.33	0.64	11220	77.0%	6.0%
F24h	-1.40	3.4×10^{-6}	0.27	0.65	24325	90.8%	3.3%
F48h	-1.39	2.8×10^{-6}	0.25	0.82	29275	92.3%	2.4%

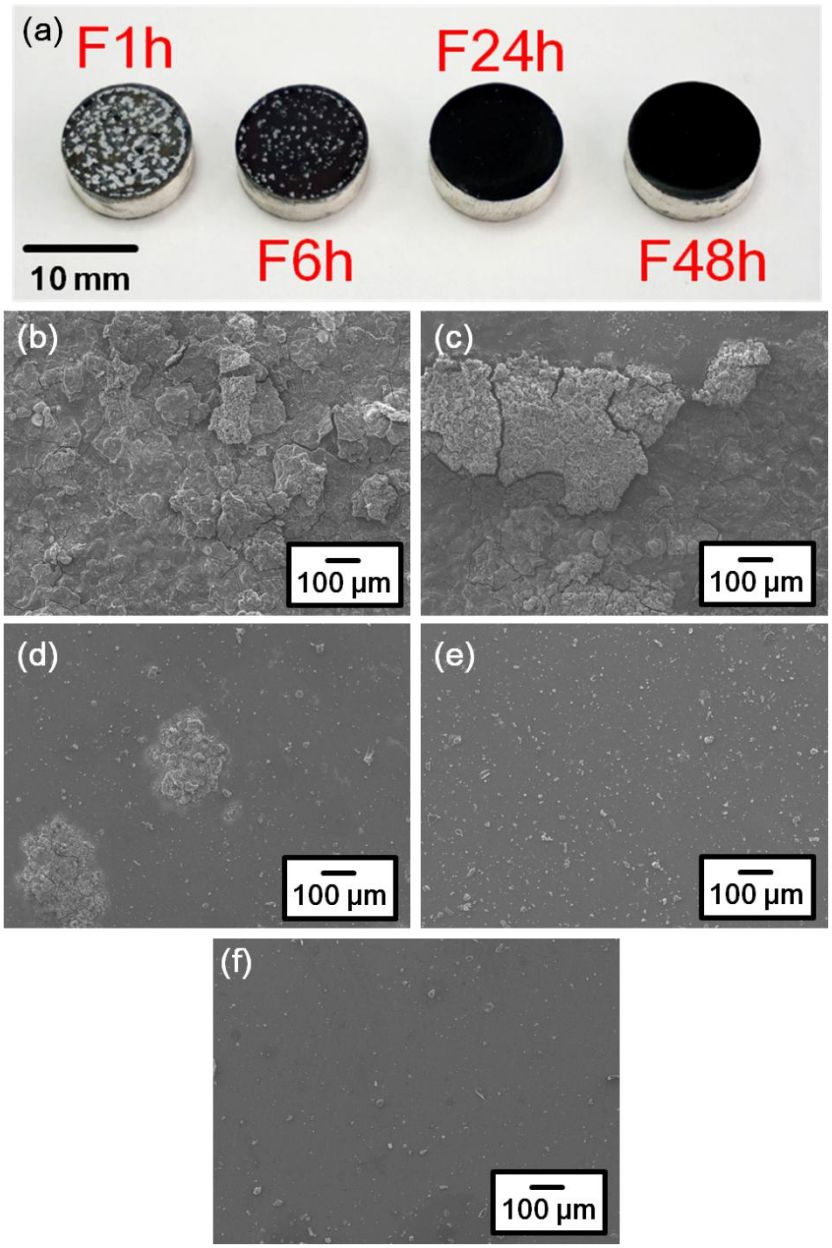

Figure 7. Electrochemically corroded surface macrograph and micrographs of the samples fluorinated for different conversion times: (a) appearance of each specimen, (b) ZK60H substrate, (c) F1h specimen, (d) F6h specimen, (e) F24h specimen, and, (f) F48h specimen.

In Figs.1 and 4, the F24h and F48h possessed a fully covered MgF_2 layer, and so showed higher corrosion resistance. Compared to the ZK60H substrate, the fluoride coating gradually increased the R_p and PE values with the increasing conversion time. Moreover, there was a significant difference at the anodic branches of the curves. In the anodic branch of the polarization curves for all specimens, a significant change in the slope is attributed to the breakdown potential (E_b) of the film surface, indicating a passive to active transition behavior [37]. This behavior provides evidence of the protective property. Notably, the E_b results can be divided into two systems. The ZK60H, F1h and F6h specimens possessed a similar E_b value, which was located at around -1.3V. In contrast, the F24h and F48h samples showed a higher level of E_b at around -1.1V; therefore, severe corrosion did not easily occur on its surface. The electrochemically corroded morphologies clearly showed that only the F24h and F48h specimens protected the substrate and prevented severe corrosion, as shown in Fig. 7.

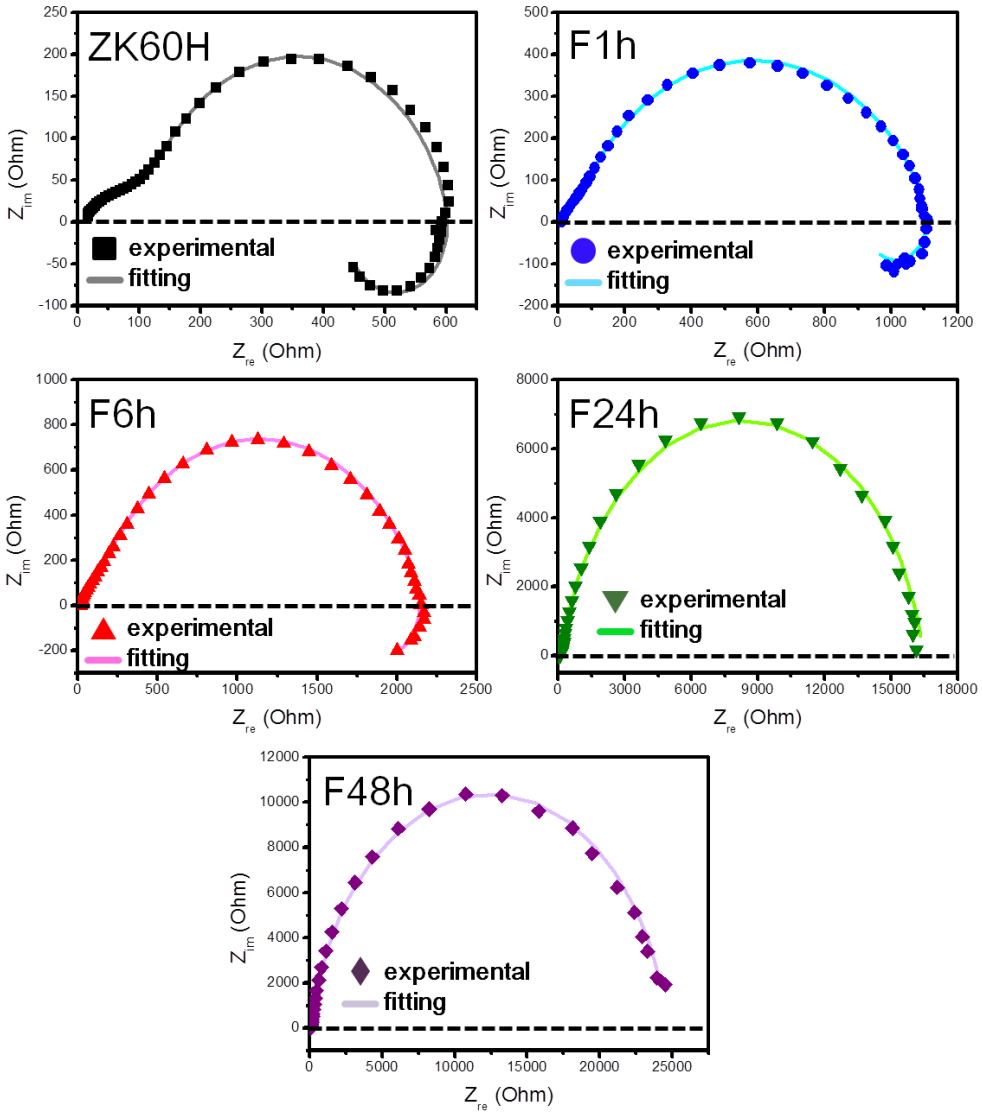

Figure 8. Nyquist curves and fitting results of the surface-coated samples obtained in r-SBF at 37 °C.

Thus, the polarization results demonstrate that the MgF_2 conversion coating with more than 24h treatment time could effectively enhance the anti-corrosion performance of ZK60 substrate.

Calculating the electrochemical parameters of the polarization test is an effective and simple method for determining coating porosity, especially for coatings that are difficult to estimate. Many studies have used the following equation for predicting coating porosity [12, 35]:

$$P_F = \frac{R_{sub}}{R_{coat}} \times 10^{-|\Delta E_{corr}/\beta_a|} \times 100\%$$

where P_F is the porosity rate of the MgF_2 layer, R_{sub} is the polarization resistance of the ZK60H substrate, R_{coat} is the polarization resistance of the MgF_2-coated specimen, E_{corr} is the difference in corrosion potential between the MgF_2 coating and the ZK60H substrate, and β_a is the anodic slope obtained from the Tafel region of the ZK60H substrate.

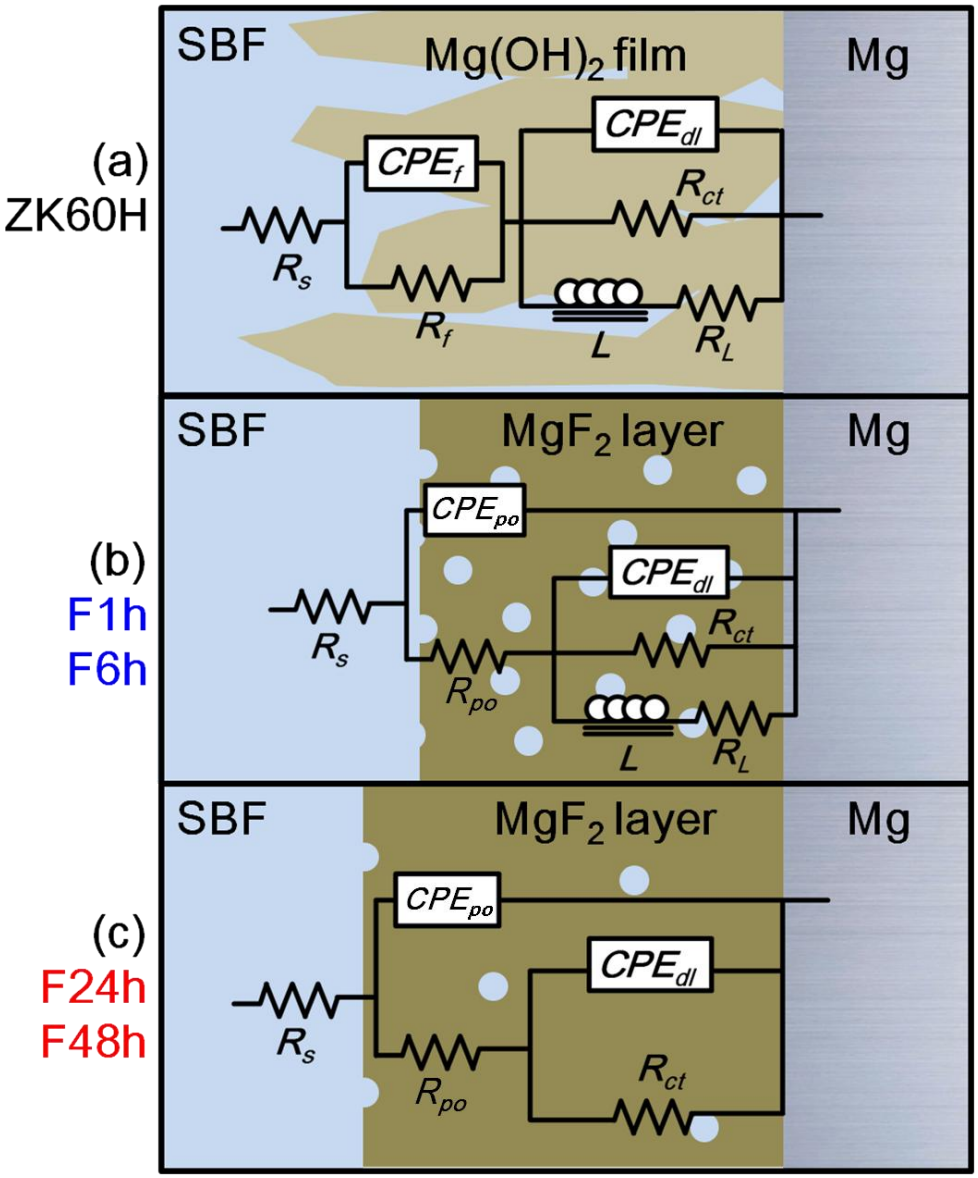

Figure 9. Schematic diagram of equivalent circuit and working electrode.

The calculated porosity values of the MgF_2 coatings are listed in table 1. Obviously, the porosities of the F24h and F48h specimens are much lower than those of the F1h and F6h samples. More importantly, the calculated results are consistent with the observed trends in the SEM and TEM images (see Figs.1 and 5). In general, pores absorb and provide the access for corrosive medium to the substrate; consequently, a lower coating porosity leads to better protection. In this respect, our polarization results show that the 3.3% or lower porosity of the MgF_2 coating provides excellent protection performance.

EIS is a powerful technique for determining the reaction between a corrosive medium and the surface film of metals and coatings [7]. In general, the capacitive arc at the high-frequency region represents the protective ability of a surface layer, while the data plots at the lower frequencies mainly result from the electrochemical corrosion process at the interface between the surface layer and substrate. As shown in Fig. 8, the capacitive arc increases with the increase of conversion time. Notably, for the F24h and F48h specimens, the high frequency data plots from the fourth quadrant of the complex plane no longer appeared, representing that the active dissolution of the matrix was prevented on these two specimens. More importantly, the trend of these results is consistent with the above-mentioned polarization results; accordingly, fluoride conversion is evidently an effective method to enhance the corrosion resistance of the ZK60H surface.

In order to better understand the corrosion mechanism of these coatings, the resultant EIS plots of the uncoated and coated specimens in the r-SBF solution were systematically analyzed through ZsimpWin 3.20 software. The fitted data of the equivalent circuits coincide well with the experimental data in all examined specimens, and the λ^2 value of all simulation results were around 10^{-3}, indicating good agreement between the fitted and experimental EIS data (Fig.9 and table 2).

Table 2. Fitting results of equivalent circuit elements.

	R_s (Ω-cm^2)	CPE_f-Y_0 ($S\cdot s^n/cm^2$)	n	R_f (Ω-cm^2)	CPE_{po}-Y_0 ($S\cdot s^n/cm^2$)	n	R_{po} (Ω-cm^2)	CPE_{dl}-Y_0 ($S\cdot s^n/cm^2$)	n	R_{ct} (Ω-cm^2)	L (H-cm^2)	R_L (Ω-cm^2)	λ^2
ZK60H	9.73	$3.2x10^{-5}$	0.60	118.3	---	---	---	$4.1x10^{-5}$	0.86	478.9	$0.7x10^4$	847	$6.1\ x10^{-4}$
F1h	10.21	---	---	---	$1.3x10^{-5}$	0.81	115.9	$2.8x10^{-5}$	0.78	994.2	$4.1x10^4$	4051	$5.4\ x10^{-4}$
F6h	10.51	---	---	---	$1.1x10^{-5}$	0.81	276.4	$2.3x10^{-5}$	0.77	1882	$1.6x10^5$	6203	$8.4\ x10^{-4}$
F24h	8.23	---	---	---	$2.4x10^{-5}$	0.89	198.5	$1.9x10^{-5}$	0.80	$1.6x10^4$	---	---	$1.1\ x10^{-3}$
F48h	9.21	---	---	---	$3.2x10^{-5}$	0.80	42.07	$2.2x10^{-5}$	0.88	$2.5x10^4$	---	---	$3.0\ x10^{-3}$

R_s represents the solution resistance between the reference electrode and the working electrode, and reflects the conductivity of the solution and the surface geometry of the working electrode. In order to better describe the behavior of the inhomogeneity and surface diffusion factor of the electrode surface, the constant phase element (CPE) is used to replace the capacitor [38]. In the present study, all experimental EIS data can be divided into three kinds of equivalent circuit system. For the surface of the ZK60H substrate, the CPE_f and R_f respectively represent the capacitance and resistance of the partial protective oxide and/or hydroxide films intrinsically formed on the ZK60H substrate in the r-

SBF. More specifically, R_{ct} and CPE_{dl} represent the charge transfer resistance and electric double layer capacity at the interface, respectively. Furthermore, there is an inductive loop in the low frequency range, which can be caused by the breakdown of the surface film or relaxation of the adsorbed and/or desorbed monovalent compounds [39], such as non-protective Mg(OH) or MgH intermediate oxidation products [40, 41]. Due to the fluoride-coated surfaces possessing few micro-pores (as shown in Fig.1), the R_{po} and CPE_{po} are used to represent the electrochemical characteristics in the high frequency region. Moreover, a parallel multi-element circuit composed by CPE_{dl} , R_{ct} , L, and R_L , is placed in series with R_{po} to represent the pitting corrosion behavior [12]. This fact can be connected with the severe corrosion morphology of the F1h and F6h specimens (Fig.7). Comparatively, it can be seen that the equivalent circuit models of the F24h and F48h specimens not only showed the highest R_{ct} value, but also eliminated the inductance effect.

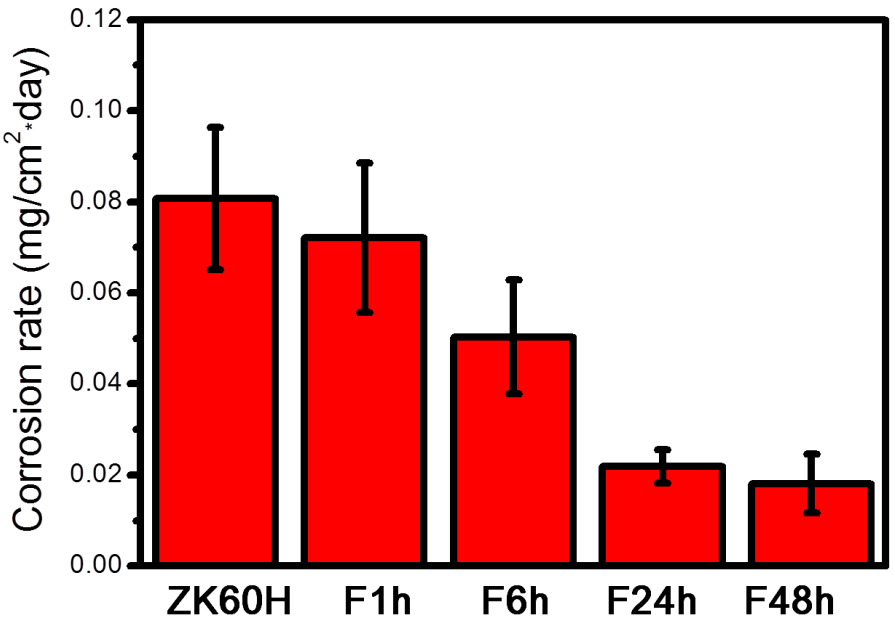

Figure 10. Corrosion rates calculated from immersion test.

The individual impedance value of the equivalent circuit model for the fluoride-coated surface shows an order as following: $R_s < R_p < R_{ct}$, which indicates that the inner layer of the MgF_2 coating contributed the most to the corrosion protection. R_{ct} acts as a dominant factor which can explain the electron exchange or oxidation of the specimens [42]. The values of R_{ct} for the F24h and F48h specimens (namely $1.6x10^4$ and $2.5x10^4$ $\Omega \cdot cm^2$) are much higher than those of the ZK60H substrate, and the F1h and F6h specimens, which are, 478.9, 994.2 and 1882 $\Omega \cdot cm^2$, respectively. In general, the larger the R_{ct} value, the higher the protection ability; moreover, the interface of the F24h and F48h specimens showed a stable status instead of active dissolution. As such, our results suggest that the F24h specimen possessed good practicability with minimum required treatment time and satisfactory performance.

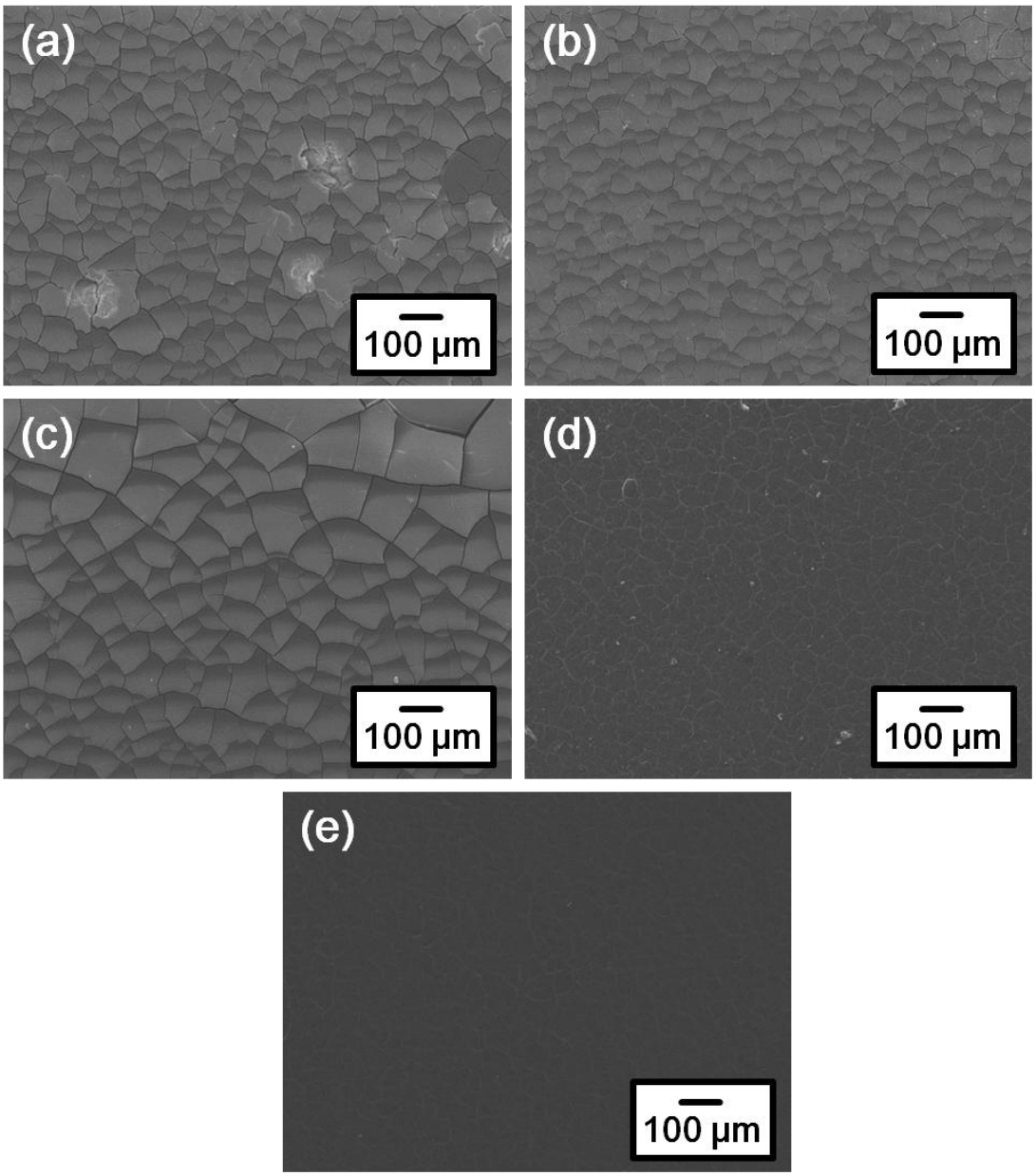

Figure 11. Corrosion morphologies of the samples fluorinated for different conversion times: (a) ZK60H substrate, (b) F1h specimen, (c) F6h specimen, (d) F24h specimen, (e) F48h specimen.

Figs.10 and 11 present the corrosion rate and morphology following the immersion test. After immersion in r-SBF for 1 week, relatively higher degradation rates for the ZK60H, F1h and F6h specimens were found, which suffered aggressive oxidation by chlorine and other reactive ions. As previously reported in the literature, $Mg(OH)_2$ is usually formed on the surface of magnesium alloys after immersion in a physiological environment [43]. However, the molar volume of the native hydroxide is much higher than magnesium [44], which caused a crack-rich corrosion layer and could not provide sufficient protection for the ZK60H substrate (Fig. 11). For the F1h and F6h specimens, due to its coating comprising a thin and porous structure, the newly formed hydroxide and/or other corrosion products dented the MgF_2 film and further caused coating fragmentation. Interestingly, the porosity variation significantly altered the corrosion morphology, with the F6h specimen showing a

larger area of corroded coating than both the ZK60H and F1h samples. Accordingly, it can be reasonably predicted that a coating with less porosity provides less opportunity for corrosive media to penetrate into the coating-substrate interface. Notably, the F24h and F48h specimens showed a promising corrosion morphology with low corrosion rates and low crack densities.

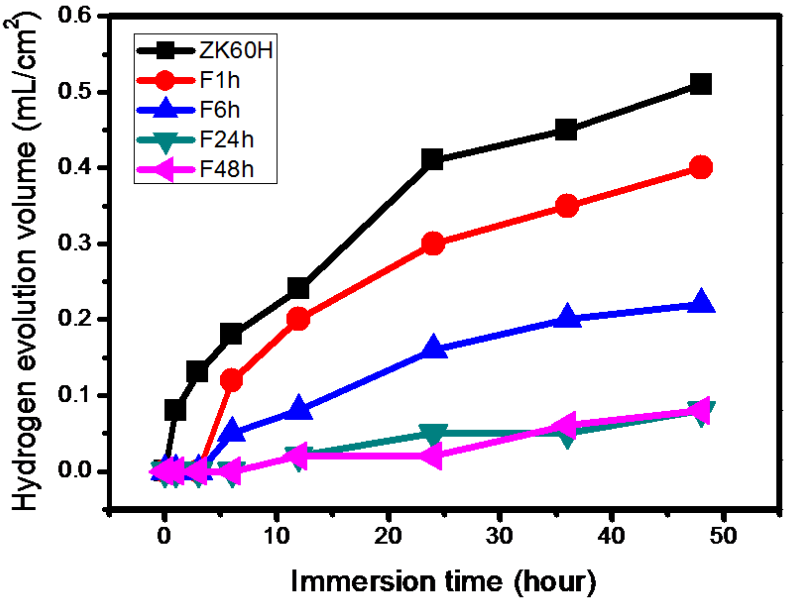

Figure 12. Hydrogen evolution curves of each specimen at 37 °C in r-SBF.

Fig.12 presents the hydrogen evolution results of the ZK60H, F1h, F6h, F24h and F48h specimens in the r-SBF measured at 37°C. The volume of evolved hydrogen gas can be correlated to the corrosion rate. Among the three different model types (equivalent circuit) of coating structure from the electrochemical test, the F24h and F48h samples not only demonstrated the highest corrosion resistance, but also exhibited the lowest hydrogen evolution volume during the testing period. Moreover, the hydrogen evolution test presented the same tendency as the electrochemical test and immersion test. Most importantly, is that the hydrogen evolution phenomenon of biomedical Mg-Zn-Zr alloys can be minimized through a proper fluoride conversion process (at least 24hr). This duplex modified magnesium material with a homogenous microstructure and satisfactory surface properties shows potential for practical applications in the biomedicine field.

3.3 Optical characteristics and non-destructive evaluation

MgF_2 has a low refractive index (n=1.38, at the wavelength of 550nm), and so could be applied in the optical anti-reflection field [45, 46]. Many previous studies have investigated the optical properties of MgF_2 coatings on different substrates and evaluated their applicability for various engineering purposes (such as solar cells and optical lenses) [47-49]. Fig.13 shows the measured surface reflectance spectra (200~800nm) on fluorinated ZK60H substrate for different conversion

times (1hr~48hr). The spectra of visible light reflected from the ZK60H substrate and F1h sample display optical interference fringe characteristics, due to the surface film (native oxide for ZK60H and thin MgF_2 film for F1h) thicknesses reaching a similar order of wavelength of visible light. Notably, the spectra show that the reflectance decreases with increasing conversion time; moreover, only the F24h and F48h specimens achieved a broadband low reflection. Owing to the material nature of significant refractive index variation at different wavelength. Therefore, the reflectance at fixed wavelength (550nm) for each groups are chose and discussed in the following section.

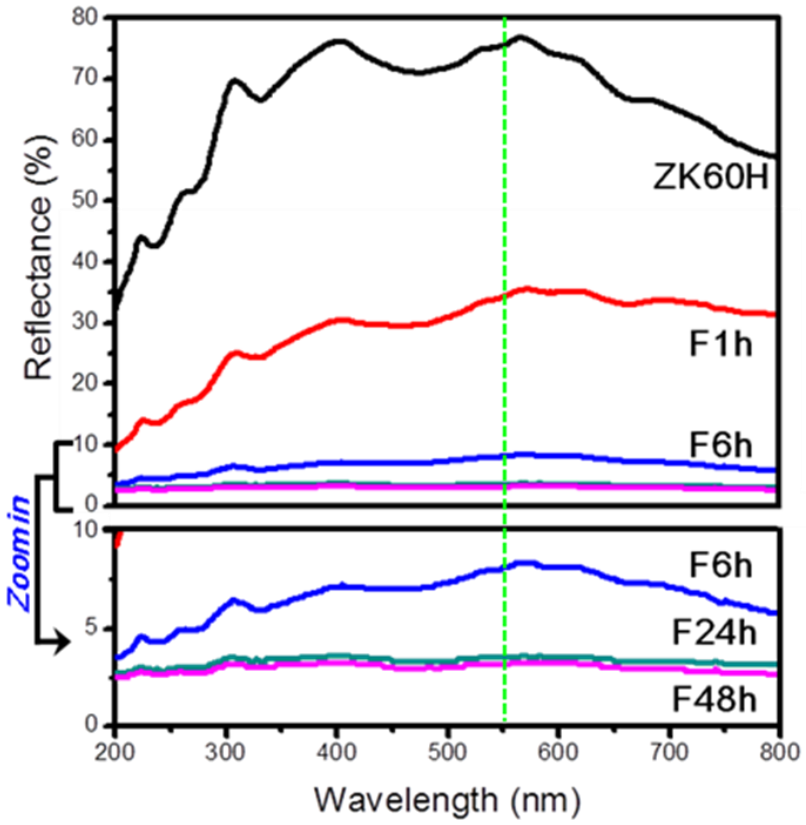

Figure 13. Optical reflectance spectrum of each specimen. (green dash line: 550nm)

Fig.14 demonstrates the correlation between PE value and reflectance, in which PE shows logarithmic growth that increases quickly in the beginning, but the gains become more difficult as conversion time goes on. In contrast, reflectance decreased with conversion time. Aggerbeck et al. suggested that the internal intermetallic particles and partly oxidized metal in a surface film increase the optical absorption and, consequently, reduce reflection [50]. Moreover, it has been proved that film microstructures such as grain boundary can cause a decrease in the reflectance value [51, 52]. In these respects, the observations from the TEM image (Fig. 5a) support these phenomenon, where several nano-$MgZn_2$ precipitates and partly fluorinated Mg granules co-exist in the MgF_2 coating thereby causing an additional reflectance reduction. The thicker fluoride film on magnesium alloy can provide better corrosion resistance than thin fluoride film [14]. The thickened film also accompanied with more $MgZn_2$ precipitate which caused additional optical absorption. Therefore, to measure the optical

reflectance can detect the fine optical variations for evaluating coating characteristics(such as thickness and anticorrosion performance). Evidently, both the PE and reflectance values stabilized after 24h. To quantify the anti-corrosion performance of the MgF_2 coating that could be expected for a given change in reflectance, a series of optical and electrochemical measurement experiments were performed. The PE value is presented as a function of reflectance in Fig. 15. Clearly, all these data plots comply with linear regression. There are two regression lines with different slopes, the inflection point of which is clearly located at 6h. As previously discussed, the coating structure affects its corresponding optical and corrosion properties. Hence, the 6h specimen acted as the turning point by implying two forming stages of MgF_2 coating within the investigated reflectance range.

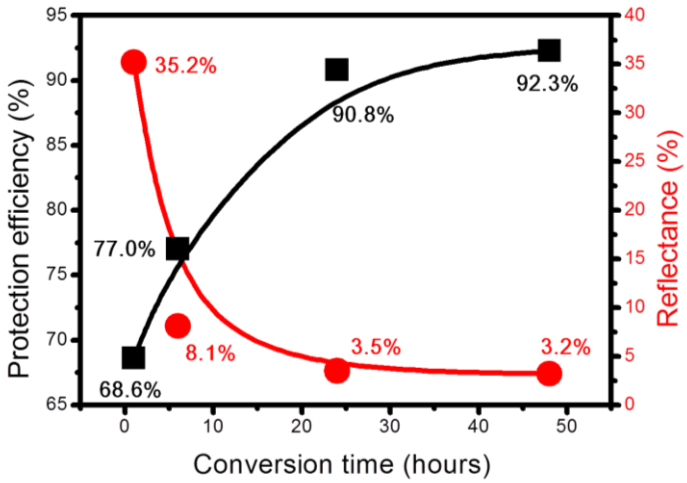

Figure 14. Combined diagram of protection efficiency, reflectance and their correlation with conversion time.

As seen in Fig.16, in the first stage of coating growth from 1h~6h (growth stage), the micro-galvanic effect played an important role in accelerating the oxidation of the α-Mg. Mg ions and hydroxide are rapidly converted to MgF_2 nano-particles. The unsealed micro-pores and non-fluorinated matrix of the thin coating not only provided a channel for aggressive ions to ingress toward the ZK60H matrix, but also reflected more incidence light, resulting in a non-ideal protection ability and relatively high reflectance value. With a prolonged deposition time (6h~24h, sealing stage) for a more stable MgF_2 coating on the ZK60H substrate, the surface was sealed and became homogeneous; as a consequence, the obstacle effect of potential difference between the α-Mg matrix and $MgZn_2$ phases gradually became smaller and the micro-galvanic effect was minimized. In other words, the corrosion trend and driving force decreased. Meanwhile, the evenly-covered MgF_2 surface caused a lower reflectance value, primarily because the non-fluorinated Mg granules were no longer exposed to environment and so the light reflection was reduced. Therefore, we could say that, the closer the reflectance value approaches the limit (~3.2%), the better the anti-corrosion performance will be (PE~90%). Consequently, through comparing the electrochemical and optical measurements of the coated Mg-Zn alloy, our results provide an index as a non-destructive method for predicting the anti-corrosion performance of MgF_2 coatings on ZK60H substrate.

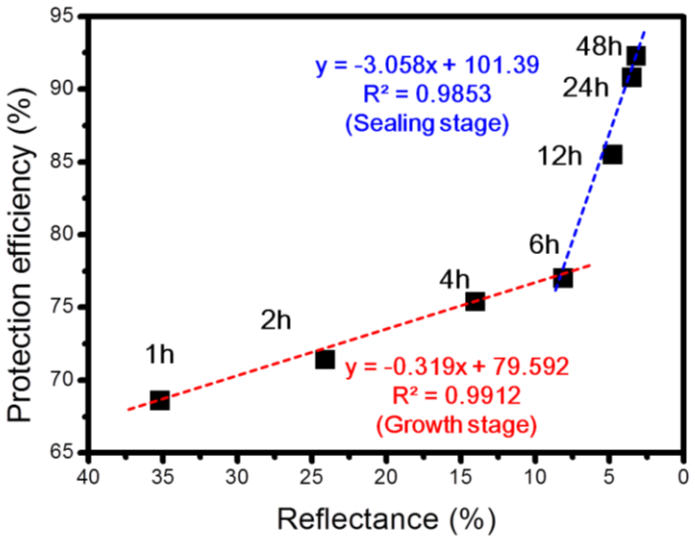

Figure 15. Relation between protection efficiency and reflectance. The two trend lines indicate the two stages (growth and sealing stage) of coating formation.

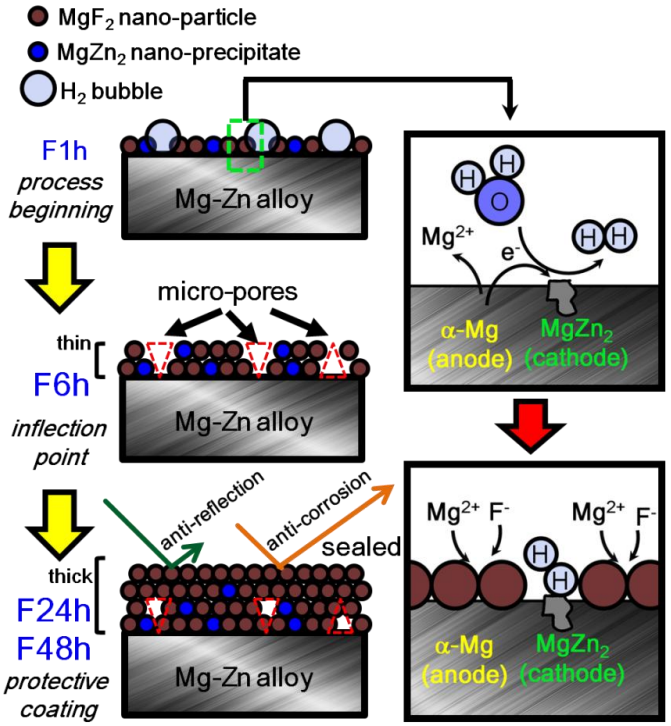

Figure 16. Schematic representation of coating growth and characteristics.

4. CONCLUSION

Fluoride conversion treatment is a simple, low cost and promising method for surface modification of biomedical magnesium alloys. This study proposed a coating mechanism of applying nano-MgF_2 film on microstructure-modified ZK60 alloy and verified the feasibility. The results show

that nano-sized MgF_2 and $MgZn_2$ are the main components of the coatings. The anti-corrosion performance (including corrosion rate and corrosion behavior) of the coatings can be significantly improved by optimizing the conversion time. The F24h specimen showed the best practical potential with satisfactory performance and reasonable processing time. Moreover, the relation between optical reflectance and protection ability was reported for the first time in this paper. Moreover, the reflectance value can provide pertinent information regarding both the growth stage and sealing stage of the fluoride coating on the Mg-Zn-Zr alloy. In summary, the fluoride coating obtained from the conversion time of 24h exhibited a 3.5% reflectance, which corresponds to over 90% protection efficiency thereby providing an index for non-destructive evaluation in simulated biological corrosive environments.

ACKNOWLEDGEMENTS
The authors are grateful to the Instrument Center of National Cheng Kung University and Southern Taiwan Medical Device Industry Cluster, AZ-10-16-35-105, for their financial support of this research.

References

1. R. K. Rude, H. E. Gruber, H. J. Norton, L. Y. Wei, A. Frausto and J. Kilburn, *Bone*, 37 (2005) 211.
2. K. He, K. Liu, M. L. Daviglus, S. J. Morris, C. M. Loria, L. Van Horn, D. R. Jacobs and P. J. Savage, *Circulation*, 113 (2006) 1675.
3. D. J. Lin, F. Y. Hung, T. S. Lui and M. L. Yeh, *Mat. Sci. Eng. C-Mater. Biol. Appl.*, 51 (2015) 300.
4. S. X. Zhang, X. N. Zhang, C. L. Zhao, J. A. Li, Y. Song, C. Y. Xie, H. R. Tao, Y. Zhang, Y. H. He, Y. Jiang and Y. J. Bian, *Acta Biomater.*, 6 (2010) 626.
5. H. R. B. Rad, M. H. Idris, M. R. A. Kadir and S. Farahany, *Mater. Des.*, 33 (2012) 88.
6. D. Q. Fang, X. J. Li, H. Li and Q. M. Peng, *Int. J. Electrochem. Sci.*, 8 (2013) 2551.
7. N. T. Kirkland, N. Birbilis and M. P. Staiger, *Acta Biomater.*, 8 (2012) 925.
8. Y. Xin, T. Hu and P.K. Chu, *Acta Biomater.*, 7 (2011) 1452.
9. F. Witte, *Acta Biomater.*, 6 (2010) 1680.
10. D. J. Lin, F. Y. Hung, M. L. Yeh and T. S. Lui, *J. Mater. Sci.-Mater. Med.*, 26 (2015) 248.
11. F. Rosalbino, S. De Negri, A. Saccone, E. Angelini and S. Delfino, *J. Mater. Sci.-Mater. Med.*, 21 (2010) 1091.
12. D. J. Lin, F. Y. Hung, S. Jakfar and M. L. Yeh, *Mater. Des.*, 89 (2016) 235.
13. X. B. Chen, N. Birbilis and T. B. Abbott, *Corrosion*, 67 (2011) 035005.
14. T. T. Yan, L. L. Tan, D. S. Xiong, X. J. Liu, B. C. Zhang and K. Yang, *Mat. Sci. Eng. C-Mater. Biol. Appl.*, 30 (2010) 740.
15. M. H. Kang, T. S. Jang, S. W. Kim, H. S. Park, J. Song, H. E. Kim, K. H. Jung and H. D. Jung, *Mat. Sci. Eng. C-Mater. Biol. Appl.*, 62 (2016) 634.
16. R. C. Zeng, Z. D. Lan, L. H. Kong, Y. D. Huang and H. Z. Cui, *Surf. Coat. Technol.*, 205 (2011) 3347.
17. M. Mosialek, G. Mordarski, P. Nowak, W. Simka, G. Nawrat, M. Hanke, R. P. Socha and J. Michalska, *Surf. Coat. Technol.*, 206 (2011) 51.
18. B. J. Han, D. D. Gu, Y. Yang, L. Fang, G. H. Peng and C. B. Yang, *Int. J. Electrochem. Sci.*, 11 (2016) 10779.
19. L. Li, Q. Qu, Z. W. Fang, L. Wang, Y. W. He, R. Yuan and Z. T. Ding, *Int. J. Electrochem. Sci.*, 7 (2012) 12690.
20. A. R. Shashikala, R. Umarani, S. M. Mayanna and A. K. Sharma, *Int. J. Electrochem. Sci.*, 3 (2008) 993.

21. K. Y. Chiu, M. H. Wong, F. T. Cheng and H. C. Man, *Surf. Coat. Technol.*, 202 (2007) 590.
22. S. M. G. Farley, J. E. Wergedal, L. C. Smith, M. W. Lundy, J. R. Farley and D. J. Baylink, *Metab.-Clin. Exp.*, 36 (1987) 211.
23. A. Drynda, T. Hassel, R. Hoehn, A. Perz, F. W. Bach and M. Peuster, *J. Biomed. Mater. Res. Part A*, 93A (2010) 763.
24. F. Witte, J. Fischer, J. Nellesen, C. Vogt, J. Vogt, T. Donath and F. Beckmann, *Acta Biomater.*, 6 (2010) 1792.
25. M. Thomann, C. Krause, N. Angrisani, D. Bormann, T. Hassel, H. Windhagen and A. Meyer-Lindenberg, *J. Biomed. Mater. Res. Part A*, 93A (2010) 1609.
26. T. T. Yan, L. L. Tan, B. C. Zhang and K. Yang, *J. Mater. Sci. Technol.*, 30 (2014) 666.
27. R. Ambat and W. Zhou, *Surf. Coat. Technol.*, 179 (2004) 124.
28. N. V. Phuong, S. Moon, D. Chang and K. H. Lee, *Appl. Surf. Sci.*, 264 (2013) 70.
29. Y. Lu, A. R. Bradshaw, Y. L. Chiu and I. P. Jones, *J. Alloy. Compd.*, 614 (2014) 345.
30. N. Zidane, A. A. Addi, R. A. Akbour, J. Douch, R. N. Singh and M. Hamdani, *Int. J. Electrochem. Sci.*, 10 (2015) 9395.
31. M. C. Zhao, M. Liu, G. L. Song and A. Atrens, *Corrosion Sci.*, 50 (2008) 1939.
32. F. Witte, J. Fischer, J. Nellesen, H. A. Crostack, V. Kaese, A. Pisch, F. Beckmann and H. Windhagen, *Biomaterials*, 27 (2006) 1013.
33. G. S. Frankel, A. Samaniego and N. Birbilis, *Corrosion Sci.*, 70 (2013) 104.
34. M. Stern and A. L. Geary, *J. Electrochem. Soc.*, 104 (1957) 56.
35. M. Fouladi and A. Amadeh, *Electrochim. Acta*, 106 (2013) 1.
36. J. E. Gray and B. Luan, *J. Alloy. Compd.*, 336 (2002) 88.
37. H. Hornberger, S. Virtanen and A. R. Boccaccini, *Acta Biomater.*, 8 (2012) 2442.
38. J. B. Jorcin, M. E. Orazem, N. Pebere and B. Tribollet, *Electrochim. Acta*, 51 (2006) 1473.
39. M. Razavi, M. Fathi, O. Savabi, B. H. Beni, D. Vashaee and L. Tayebi, *Ceram. Int.*, 40 (2014) 9473.
40. G. Song, A. Atrens, D. St John, X. Wu and J. Nairn, *Corrosion Sci.*, 39 (1997) 1981.
41. R. Pinto, M. G. S. Ferreira, M. J. Carmezim and M. F. Montemor, *Electrochim. Acta*, 56 (2011) 1535.
42. M. Jamesh, S. Kumar and T. S. N. S. Narayanan, *Corrosion Sci.*, 53 (2011) 645.
43. N. T. Kirkland, J. Lespagnol, N. Birbilis and M. P. Staiger, *Corrosion Sci.*, 52 (2010) 287.
44. J. Chen, J. Q. Wang, E. H. Han, J. H. Dong and W. Ke, *Electrochim. Acta*, 52 (2007) 3299.
45. M. J. Dodge, *Appl. Optics*, 23 (1984) 1980.
46. T. Murata, H. Ishizawa, I. Motoyama and A. Tanaka, *J. Sol-Gel Sci. Technol.*, 32 (2004) 161.
47. H. K. Raut, S. S. Dinachali, K. K. Ansah-Antwi, V. A. Ganesh and S. Ramakrishna, *Nanotechnology*, 24 (2013) 505201.
48. Y. M. Wan, C. Samundsett, J. Bullock, T. Allen, M. Hettick, D. Yan, P. T. Zheng, X. Y. Zhang, J. Cui, J. McKeon, A. Javey and A. Cuevas, *ACS Appl. Mater. Interfaces*, 8 (2016) 14671.
49. S. K. Dhungel, J. Yoo, K. Kim, S. Jung, S. Ghosh and J. Yi, *J. Korean Phys. Soc.*, 49 (2006) 885.
50. M. Aggerbeck, A. Junker-Holst, D. V. Nielsen, V. C. Gudla and R. Ambat, *Surf. Coat. Technol.*, 254 (2014) 138.
51. Y. Zhang, *Dent. Mater.*, 30 (2014) 1195.
52. H. L. Zhu, X. Q. Zhang, M. J. Couper and A. K. Dahle, *Mater. Chem. Phys.*, 113 (2009) 401.